Scanning Rayleigh Doppler Lidar for Wind Profiling Based on Non-polarized Beam Splitter Cube Optically Contacted FPI

**Jun Zheng, Dongsong Sun*, Tingdi Chen, Ruocan Zhao,
Yuli Han, Zimu Li, Anran Zhou, and Nannan Zhang**

*CAS Key Laboratory of Geospace Environment, University of Science and Technology of China,
Hefei, 230026, China*

A Scanning Rayleigh Doppler lidar for wind profiling based on a non-polarized beam splitter cube optically contacted FPI is developed for wind measurement from high troposphere to low stratosphere in 5-35 km. Non-polarized beam splitter cube optically contacted to the FPI are used for a stable optical receiver. Zero Doppler shift correction is used to correct for laser or FPI frequency jitter and drift and the timing sequence is designed. Stability of the receiver for Doppler shift discrimination is validated by measuring the transmissions of FPI in different days and analyzed the response functions. The maximal relative wind deviation due to the stability of the optical receiver is about 4.1% and the standard deviation of wind velocity is 1.6% due to the stability. Wind measurement comparison experiments were carried out in Jiuquan (39.741°N, 98.495°E), Gansu province of China in 2015, showing good agreement with radiosonde result data. Continuous wind field observation was performed from October 16th to November 12th and semi-continuous wind field of 19 nights are presented.

Keywords : Rayleigh Doppler lidar, Zero Doppler shift correction, Stability validation, Continuous wind field observation
OCIS codes : (280.3640) Lidar; (280.4788) Optical sensing and sensors; (280.1350) Backscattering

I. INTRODUCTION

Wind measurement is fundamental for a comprehensive understanding of atmospheric dynamics on small (<100 km) to global scales in this region [1-4]. The possibility to measure winds in the middle atmosphere with a Doppler lidar using a Fabry-Perot interferometer (FPI) was already demonstrated more than two decades ago [5-10]. Chanin *et al*. first realized the wind measurement in the stratosphere at the Observatory of Haute Provence (OHP), France in 1989. They used two high resolution and narrow bandpass Fabry-Perot interferometers as the frequency discriminator to measure the wind up to 50 km altitude [11-14]. Another system for wind measurement up to an altitude near 60 km was developed by Tepley *et al*., in which a single FPI was used for spectral scanning of the Rayleigh backscattered spectrum [15-17]. The Goddard Lidar Observatory for Winds (GLOW) mobile Doppler lidar used a double-edge FPI for stratosphere wind measurement at NASA Goddard Space Flight Center. This system choose a frequency tripled Nd:YAG laser and the wavelength of the laser was 355 nm [18]. The ALOMAR (Arctic Lidar Observatory for Middle Atmosphere Research) system observed wind by the RMR (Rayleigh/Mie/Raman) lidar in Norway. FPI and a Doppler Rayleigh Iodine Spectrometer were combined in the lidar for wind and temperature observation in the stratosphere and mesosphere up to 80 km [1, 19, 20]. In the Atmospheric Dynamics Mission Aeolus (ADM-Aeolus) payload Atmospheric Laser Doppler Instrument (ALADIN), which has been demonstrated by airborne validation, is scheduled to be launched in the near future. The observation range of stratospheric wind profiles is expected to be 0-30

---

km altitude [21-23]. Two Rayleigh Doppler lidars based on double-edge technique were set up in succession at the University of Science and Technology of China (USTC). One was for upper troposphere to stratosphere (8-40 km) wind measurement and another was developed for wind and temperature in the stratosphere to lower mesosphere (15-60 km) [24-28].

Recently, a scanning Rayleigh Doppler lidar has been set up for simultaneous high troposphere and stratosphere wind measurement from 5 km to 35 km by our group at USTC (University of Science and Technology of China). In this paper we describe the system setup in detail and present the performance of wind detection in Jiuquan, Gansu province. The lidar measurement is compared with radiosonde wind measurements taken simultaneously at the same location.

II. PRINCIPLE

The scanning Rayleigh Doppler lidar based on the double-edge technique uses the Rayleigh backscatter to take the wind measurement. According to the Doppler Effect, the wind velocity component along the line of sight (LOS) can be calculated by the equation as follow:

$$V_{LOS} = \frac{\lambda}{2} \Delta \nu \tag{1}$$

where λ is the wavelength of the outgoing laser; $\Delta \nu$ represents the Doppler shift.

In this lidar, a triple channel FPI, which is capacitively stabilized and piezoelectrically tunable is used as frequency discriminator to determine the Doppler shift of the received signal by its double-edge channels located on the wings of the thermally broadened molecular backscattered signal spectrum. The frequency of the transmitter laser is located at the cross-point of the two edge channels of the FPI. Molecular backscattered signals pass through the FPI's two edge channels. As Fig. 1 shows, the Doppler shift of the
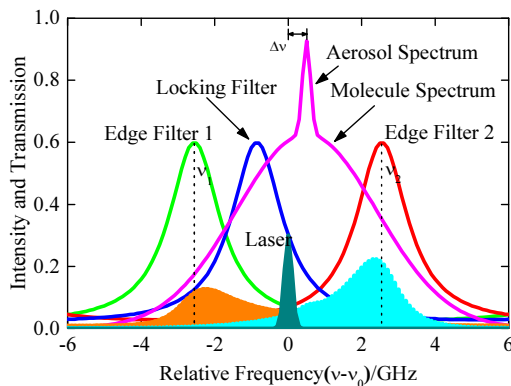

FIG. 1. Schematic of the principle of Doppler shift determination using a triple channel FPI.

signal will cause the transmission of one edge channel to increase and the other one to decrease. The Doppler shift can be calculated by detecting the signals of the two edge channels.

The response function for wind retrieval at each altitude z is defined as:

$$R(\Delta \nu) = \frac{aI_1(\nu_1, \nu_l + \Delta \nu) - I_2(\nu_2, \nu_l + \Delta \nu)}{aI_1(\nu_1, \nu_l + \Delta \nu) + I_2(\nu_2, \nu_l + \Delta \nu)} \tag{2}$$

where $I_1(\nu_1, \nu_l+\Delta\nu)$ and $I_2(\nu_2, \nu_l+\Delta\nu)$ are the signal intensity from altitude z detected through the edge 1 and edge 2 channel with a Doppler shift $\Delta\nu$, respectively. In this system, signal intensity is equal to the number of photons detected by the PMTs operated in photon counting mode; a is the corrective factor introduced to account for the possible imbalance between the double-edge channels; v1 and v2 are the center frequency of the edge channels, and vl is the laser center frequency. Besides, the I1(v1, vl+Δv) and I2(v2, vl+Δv) are considered as convolution of the laser spectrum, Rayleigh backscattering spectrum and the function of the FPI edge channel transmission if we ignored the aerosol backscattering.

$$I_1(\nu_1, \nu_l + \Delta \nu) = \int_{-\infty}^{\infty} I_L(\nu) T_1 (\nu - \nu_1) I_R \left[\nu - (\nu_l + \Delta \nu)\right] d\nu$$
$$I_2(\nu_2, \nu_l + \Delta \nu) = \int_{-\infty}^{\infty} I_L(\nu) T_2 (\nu - \nu_2) I_R \left[\nu - (\nu_l + \Delta \nu)\right] d\nu \tag{3}$$

where $I_L(\nu)$ is the outgoing laser spectrum; $T_1(\nu)$ and $T_2(\nu)$ are the transmission functions of the FPI's two edge channels; $I_R(\nu)$ is the Rayleigh backscattering spectrum. This can deduce the Doppler shift profile $\Delta\nu$ from the response profile $R(\Delta\nu)$ through the instrumental calibration function by accounting for the atmospheric temperature depended Rayleigh backscattering spectrum profile.

The wind velocity along the line of sight (LOS) is calculated as:

$$V_{LOS} = \frac{\lambda}{2} \frac{d\nu}{dR(\nu)} [R(\Delta \nu) - R(0)] \tag{4}$$

In this equation, $R(0)$ is the response without Doppler shift. It can be measured by zero Doppler shift correction described below.

III. LIDAR SYSTEM SETUP

The scanning lidar built for 5 km to 35 km wind measurement is described in this section and the key parameters of the system are summarized. The stability of the optical receiver using a non-polarized beam splitter cube NPBS is validated by a regular transmission measurement over 36 days.

3.1. Description of the Lidar System

The scanning Rayleigh Doppler is named USTC 800 lidar by us because of using a telescope with diameter 800 mm. The optical schematic view of USTC 800 lidar is given in Fig. 2.

The USTC 800 lidar employs a Q-switched, flash-pumped and frequency tripled Nd:YAG laser (INNOLAS Spitlight 2000) working at 355 nm. This laser is made stable single longitudinal mode by the injection of a very narrow bandwidth fiber laser (NP Photonics SI-2000, bandwidth <5 kHz). In order to achieve a high stability, the seeder laser is in continuous operation and the output power is about 30 mW, enough for successful injection. As the frequency of the seeder laser is sensitive to the ambient temperature, the seeder laser is mounted in a thermostat with ability to thermally control at ±0.1 K to insure long-time injection stability. The output energy is approximately 300 mJ per pulse with a repetition of 50 Hz. The laser spectral shape can be considered as a Gaussian distribution with a FWHM about 200 MHz. This spectral width is much smaller than the spectral width of both the atmospheric backscattering signal and the FWHM of the edge channels of the FPI. The laser diameter is expanded by an expander from 10 mm to 150 mm to decrease the divergence angle, which of significant meaning for us to decrease the field of view (FOV), and then the background will be depressed. This is important for a distant measurement of 35 km altitude. Divergence angle of the laser after expanding is about 50 μrad.

A very small fraction of the laser beam is sampled by a beam splitter into a 0.1 m diameter integrating sphere as the signal for FPI actively locking to the laser frequency and the zero Doppler shift correction during the wind retrieval. Application of the integrating sphere is aimed to broaden the laser pulse duration time and homogenize the laser to frequency locking channel and zero Doppler shift correction channel. The duration time of the laser pulse can be broadened from ~6 ns to ~20 ns, and the laser to frequency locking channel and zero Doppler shift correction channel is more even. Longer duration time and more even beam can bring more accurate detection of the signal from the integrating sphere. The telescope with a diameter of 800 mm is used for receiving the atmospheric back-scattering signal. The laser, integrating sphere, expander and the telescope are all mounted on an instrument for scanning, and the expander and telescope are of a zenith angle of 30°. An interference filter with 0.15 nm bandwidth is used to decrease the background.

For a purpose of stable and compact system, an optical receiver combined for frequency discriminating with FPI, non-polarized beam splitter cubes (NPBS), photomultiplier tubes (PMTs) and other components is used in this lidar system. The atmospheric backscattering signal collected by telescope and separated by a non-polarized beam splitter cube. The splitting ratio is independent on the polarization of the light and is hardly varied relative to the ambient environment for a stable optical receiver. There are two incidence plates in non-polarized beam splitter cube for atmospheric backscattering signal and zero Doppler shift correction. The small fraction of laser going into the integrating sphere is divided in two parts by two fibers. The first part is led into a smaller non-polarized beam splitter cube matching to the locking channel for laser frequency locking. The second part is split by a plate beam splitter. The reflected fraction is detected by PMT-5 as the energy monitor. The transmitted fraction is led to the NPBS-1. As the light from the integrating sphere does not contain Doppler shift, this signal can be led to the edge channels for detecting the transmission of each edge channel. The zero Doppler shift correction signal is separated by a delay on time domain of the signal from the telescope.

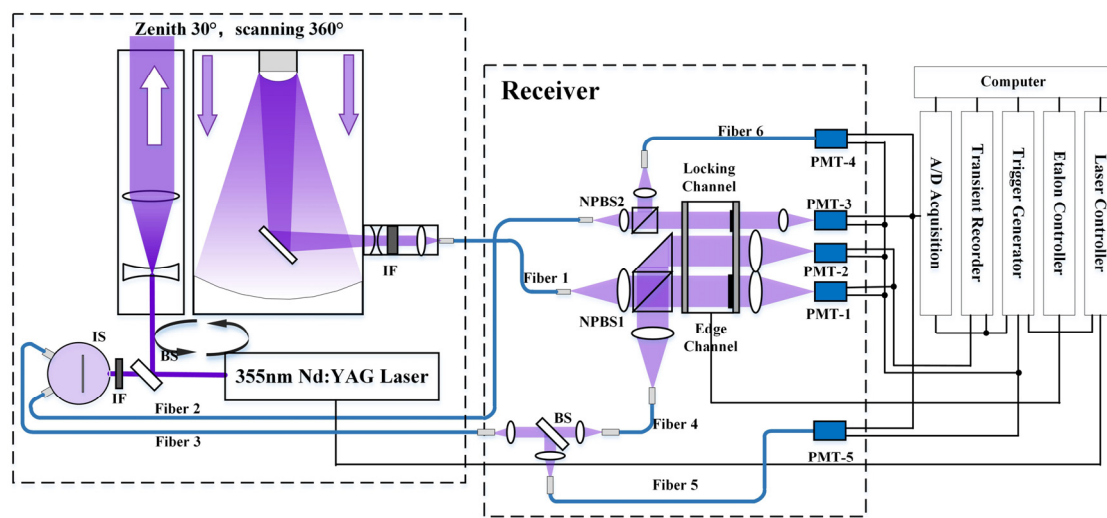The PMTs used in this system are operated in two modes.

FIG. 2. Schematic view of USTC 800 lidar. IS, integrating sphere; BS, beam splitter; IF, interference filter; NPBS, non-polarized beam splitter cube; FPI, Fabry-Perot interferometer; PMT, photomultiplier tube.

PMT-3, PMT-4 and PMT-5 are in analog mode while the two PMTs of edge channels are operated in photon counting mode. In addition, the numerical aperture (N.A.) of the fibers applied in this lidar is 0.22. The diameter of fiber 1, fiber 4, fiber 5 and fiber 6 is 200 μm while the diameter of fiber 2 and fiber 3 is 100 μm.

3.2. Zero Doppler Shift Correction

The zero Doppler shift correction is used to correct for laser or FPI frequency jitter and drift by measuring the outgoing laser transmitted from the edge channels. As Eq. (4) shows, the laser without Doppler shift measured through FPI edge channel is significant for wind retrieval. The receiver NPBS applied in generate an access to measure the zero Doppler shift signal by the FPI synchronous with the wind measurement. As edge channels are used both for the atmospheric and the correction signal, the timing sequence is designed for the measurement shown in Fig. 3. These two signals can be separated in the time domain.

It is noted that, as the zero Doppler shift correction is to measure the out-going laser by the FPI edge channels, the shape of the correction transmission curve must be same as the edge channels. Figure 4 shows the transmission curve measurement result of zero Doppler shift correction and the edge channels using a stable CW laser with the FWHM of about 1 MHz by tuning the FPI. The green symbols are the resultant data of the edge channels and the red ones indicate the zero Doppler shift correction result data. The solid line (black) and the dashed line (blue) are the fitting result using the theoretical transmission equation of the FPI as follows.

$$h(v) = T_{pe} \left(\frac{1 - R_e}{1 + R_e} \right)$$
$$\left\{ 1 + 2 \sum_{n=1}^{\infty} R_e^n \cos \left[\frac{2\pi n v}{v_{FSR}} \frac{1 + \cos \theta_0}{2} \right] \mathrm{sinc} \left[\frac{2 n v_0}{v_{FSR}} \frac{1 - \cos \theta_0}{2} \right] \right\}$$
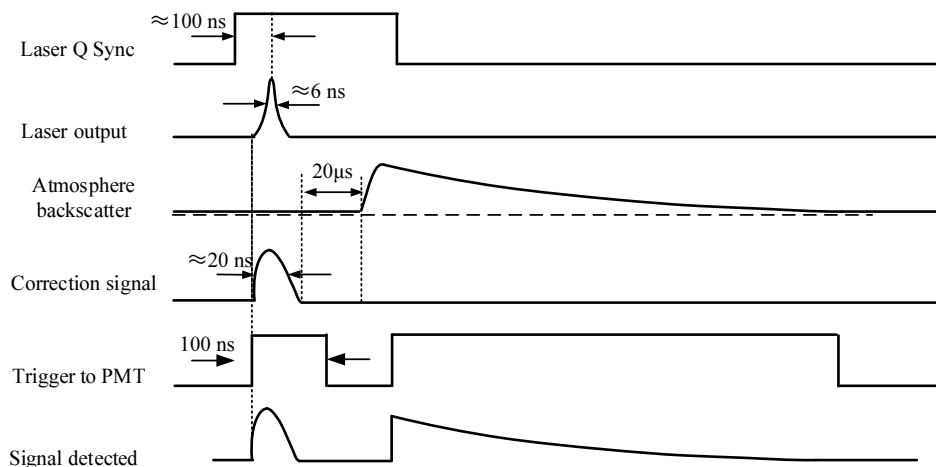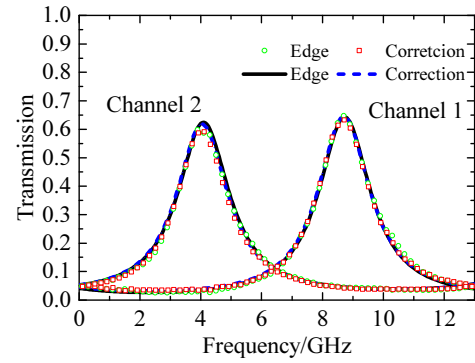
(5)

FIG. 4. Transmission curve comparison between edge channels and zero Doppler shift correction channels. The data measured is indicated as the discrete points and the solid and dashed lines are the fitting result.

TABLE 1. Key parameter of edge and correction channels fitting

	FWHM	Range of channels
Edge 1	1.934 GHz	4.907 GHz
Edge 2	1.941 GHZ	
Correction 1	1.959 GHz	4.96 GHz
Correction 2	1.933 GHz	

where T_{pe} is peak transmission; R_e is the effective reflectivity of the FPI plate; n is the refractive index of the medium between the two plates of the FPI, and in our system, the medium is air; v_{FSR} is the free spectral range (FSR) of the FPI; θ_0 is the divergence angle of the beam, in this experiment is equal to 0.5 mrad; and v_0 is the laser frequency.

From the results of the data and the fitting curve, transmissions of the edge channels and zero Doppler shift correction channel have good agreement. The key parameters of the fitting curve are listed in Table 1. The wind deviation brought by the difference between edge channels

FIG. 3. Data acquisition timing sequence.

and zero Doppler shift correction is about 0.43 m/s when the wind velocity is 100 m/s.

3.3. Stability of Optical Receiver

In the Rayleigh Doppler wind lidar, the frequency discrimination curve is significant for the Doppler shift calculation. To validate the performance of the optical receiver, the transmission of the FPI is measured in different days. These measurements were taken regularly every seven days. Figure 5(a) shows the result of the transmission measurement. It can be found that the transmission measured on different days shows good agreement. Figure 5(b) shows the standard deviation of the three channels in the FPI, and the values are all under 0.05.
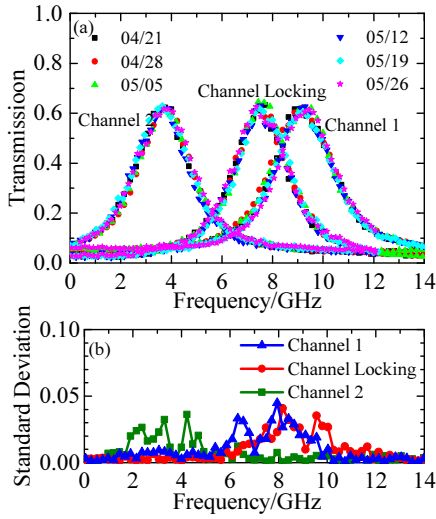

FIG. 5. (a) Transmission measurements of FPI in different days; (b) Standard deviation of the measurement.
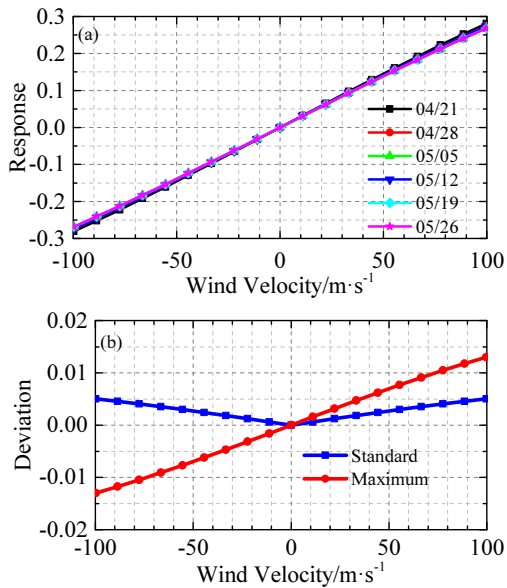

FIG. 6. Measured response (a) and deviation of the response (b) depend on the LOS velocity.

Wind velocity calculated from the response function depends on the backscatter Rayleigh spectrum and transmission of edge channels. Transmissions measured in Fig. 5 are fitted using Eq. (5). The response of each measurement is calculated and shown in Fig. 6. The standard deviation and the maximal deviation within the measurements are shown in Fig. 6(b). The maximal relative wind deviation due to the stability of the optical receiver is about 4.1% and the standard deviation of the wind velocity is 1.6%.

IV. WIND MEASUREMENT

In order to measure the horizontal wind velocity and direction, the USTC 800 lidar takes data in four direction and we assume that the vertical wind velocity is zero. During the wind detection, the optical axis is pointed from east, then west, and then south then north to measure the LOS velocity of these four directions. We assume that in the wind observation of a profile, the horizontal wind components pointing in the opposite direction is equal in value. The components of horizontal wind along the X axis (east) and Y (north) axis can be expressed as:

$$V_X = \frac{V_E - V_W}{2\sin\varphi}$$
$$V_Y = \frac{V_N - V_S}{2\sin\varphi} \tag{6}$$

In the Eq. (5), V_X and V_Y represent the components of horizontal wind along the X axis and Y axis; V_E, V_W, V_S and V_N are the LOS wind velocities of the four directions; φ is the title angle of the laser and telescope from the zenith. In this system, φ equals 30°.
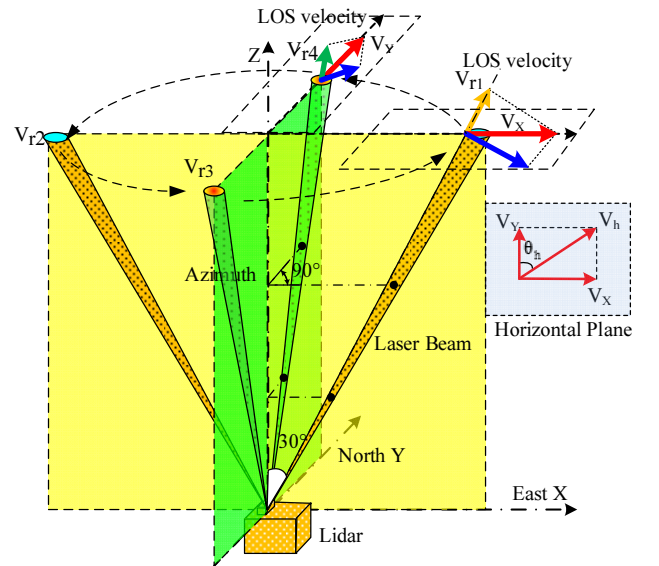

FIG. 7. Schematic diagram of the lidar wind measurement by scanning four directions.

We can calculate the horizontal wind velocity using the geometry relationship between V_X, V_Y and the horizontal velocity which showed in Fig. 7. The wind horizontal velocity V_h is expressed as a function of V_X and V_Y:

$$V_h = \sqrt{V_X{}^2 + V_Y{}^2} \qquad (7)$$

The direction of the horizontal wind θ_h can be calculated as follow:

$$\theta_h = \arctan\left(V_X / V_Y\right) + \pi\left\{1 - \text{sign}\left[V_Y + |V_Y| \cdot V_X\right]\right\} \qquad V_Y \neq 0 \qquad (8)$$

Wind measurement using the USTC 800 lidar was performed in Jiuquan (39.741°N, 98.495°E), Gansu province, northwest of China, in 2015. An example of typical raw data in the experiment is represented in Fig. 8. This raw data was taken at 13:30 UT (Universal Time), Oct. 16 in 2015. The original Rayleigh backscattering signal was indicated as a blue line and the resolution is 7.5 m. The red curve is the segmented signal with the 0.2 km (from 5 km to 15 km) and 0.5 km resolution. Accumulated time of this profile is
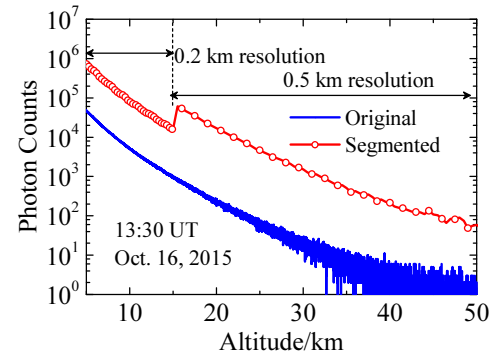

FIG. 8. Altitude profile of Rayleigh backscattering signal at 13:30 UT, Oct. 16, 2015.

30 min.

In order to validate the performance of the USTC 800 lidar based on the double-edge Rayleigh technology, radiosonde mounted on the balloon was used for wind measurement. The result of horizontal wind observation with the USTC 800 lidar is shown in Fig. 9. Radiosonde data were taken at 11:15 UT every day from 5 km to 20 km. The four altitude profiles of the wind and deviations of the two
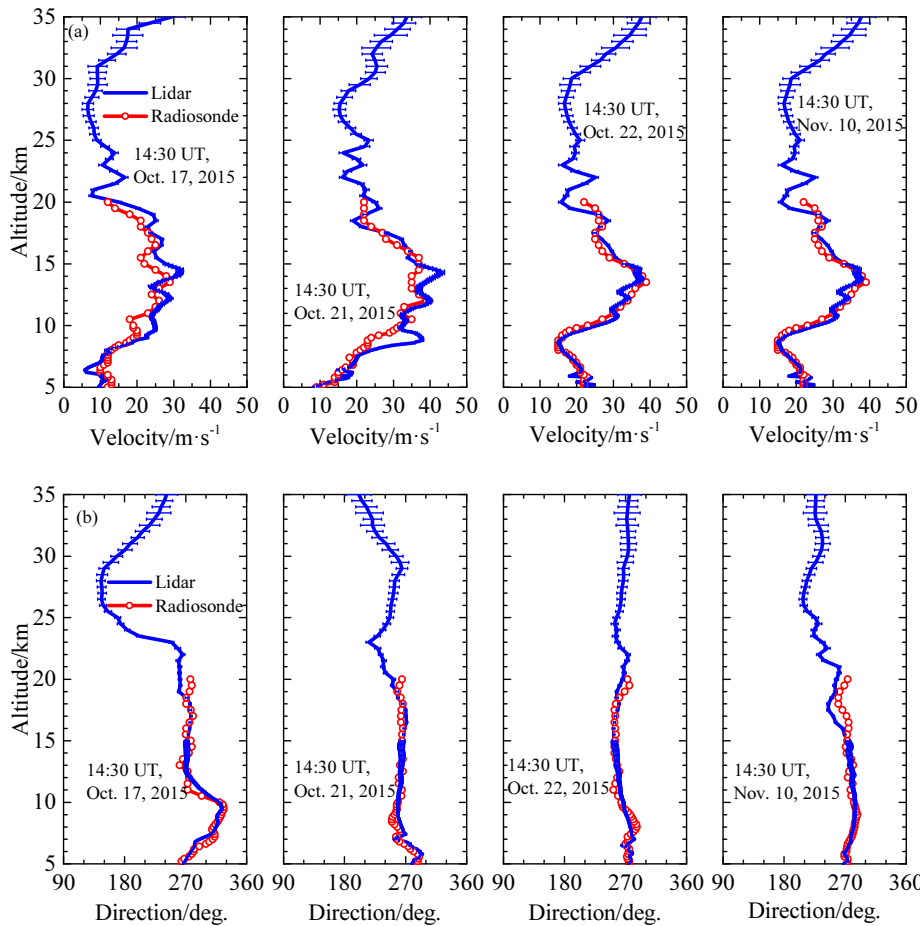

FIG. 9. (a) Horizontal wind velocity profiles and (b) direction profiles measured by the USTC 800 lidar compared with data from radiosonde at 11:15 UT.
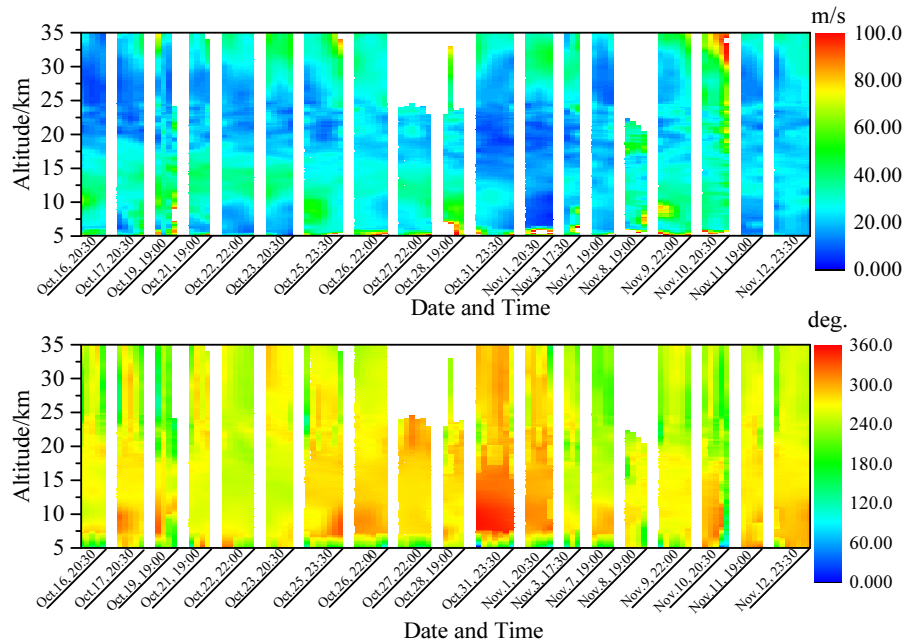
FIG. 10. Time-altitude cross section of semi-continuous horizontal wind field observation carried out from October 16th to November 12th. The wind detection we made began at 13:00 UT in each day. The date and the time shown in the figure are the ending time of wind observations. The temporal resolution of the experiment is 1.5 hours.

measurements are shown in Figs. 9(a) and 9(b). The times of lidar result data were presented in the figure and the temporal resolutions of these measurements were 1.5 h. From the result shown in Fig. 9, the result data of lidar and radiosonde have good agreement. The deviations of the wind velocity and direction are shown with error bars. In this experiment, the maximum velocity and direction measurement uncertainties are 3.9 m/s and 14.5° at 35 km altitude, respectively.

Continuous wind field observation was performed from October 16th to November 12th and the semi-continuous wind field of 19 nights is presented in Fig. 10. The distribution of the wind velocity (a) and direction (b) in high troposphere and low stratosphere is shown in the figure. The lack of the data in higher altitudes for 3 days is due to cloudy weather. Similarly to the result observed by our USTC lidar in December in 2015, the stable quasi-zero wind layer appears again from 22 to 27 km altitudes. The dynamic structure and its evolution in the atmosphere region are also clearly shown and can obtain the characteristics of the atmosphere such as gravity waves in the future analysis can be obtained similar to the Ref. 29, which has achieved the gravity wave process in middle latitudes as the second report of gravity wave using a direct detection Doppler lidar wind data [28].

V. CONCLUSION

A scanning Rayleigh Doppler lidar based on a non-polarized beam splitter cube optically contacted FPI has been set up and demonstrate for high troposphere and low stratosphere wind measurement from 5 km to 35 km. This scanning Rayleigh Doppler lidar uses a diameter of 800 mm telescope and is mounted on a support vehicle. The receiver NPBS is applied in generating an access to measure the zero Doppler shift signal by the FPI synchronous with the wind measurement. The wind deviation brought by the deference between edge channels and zero Doppler shift correction is about 0.43 m/s when the wind velocity is 100 m/s. The maximal relative wind deviation due to the stability of the optical receiver is about 4.1% and the standard deviation of wind velocity is 1.6%. Horizontal wind measurement can be realized with a spatial resolution of 100 m under 15 km and 500 m under 35 km altitude. In the comparison experiment in Jiuquan (39.741°N, 98.495°E), Gansu province of China, in 2015, wind measurement of lidar and radiosonde are in good agreement in the region from 5 km to 20 km.

REFERENCES

1. G. Baumgarten, "Doppler Rayleigh/Mie/Raman lidar for wind and temperature measurements in the middle atmosphere up to 80 km," Atmos. Meas. Tech. **3**, 1509-1518 (2010).

2. K. Salonen, G. Haase, R. Eresmaa, H. Hohtia, and H. Järvinena, "Towards the operational use of Doppler radar radial winds in HIRLAM," Atmos. Res. **10**, 190-200 (2011).

3. D. Fritts, "Gravity wave saturation in the middle atmosphere: A review of theory and observations," Rev. Geophys. Space Phys. **22**, 275-308 (1984).

4. W. Baker, R. Atlas, C. Cardinali, A. Clement, G. Emmitt, B. Gentry, R. Hardesty, E. Källén, M. Kavaya, R. Langland, Z. Ma, M. Masutani, W. McCarty, R. Pierce, Z. Pu, L. Riishojgaard, J. Ryan, S. Tucker, M. Weissmann, and J. Yoe, "Lidar measured wind profiles: the missing link in the global observing system," Am. Meteorol. Soc. **10**, 543-564 (2014).

5. C. L. Korb, B. M. Gentry, and C. Y. Weng, "Edge technique: theory and application to the lidar measurement of atmospheric wind," Appl. Opt. **31**, 4202-4213 (1992).

6. B. M. Gentry and C. L. Korb, "Edge technique for high-accuracy Doppler velocimetry," Appl. Opt. **33**, 5770-5777 (1994).

7. C. L. Korb, B. M. Gentry, and S. X. Li, "Edge technique Doppler lidar wind measurements with high vertical resolution," Appl. Opt. **36**, 5976-5983 (1997).

8. C. L. Korb, B. M. Gentry, S. X. Li, and C. Flesia, "Theory of the double-edge technique for Doppler lidar wind measurement," Appl. Opt. **37**, 3097-3104 (1998).

9. C. L. Korb, B. M. Gentry, S. X. Li, and C. Flesia, "Theory of the double-edge molecular technique for Doppler lidar wind measurement," Appl. Opt. **38**, 432-440 (1999).

10. C. Flesia, C. L. Korb, and C. Hirt, "Double-edge molecular measurement of lidar wind profiles at 355 nm," Opt. Lett. **25**, 1466-1468 (2000).

11. M. L. Chanin, A. Garnier, A. Hauchecorne, and J. Porteneuve, "A Doppler lidar for measuring winds in the middle atmosphere," Geophys. Res. Lett. **16**, 1273-1276 (1989).

12. A. Garnier and M. L. Chanin, "Description of a Doppler Rayleigh lidar for measuring winds in the middle atmosphere," Appl. Phys. B **55**, 35-40 (1992).

13. C. Souprayen, A. Garnier, A. Hertzog, A. Hauchecorne, and J. Porteneuve, "Rayleigh-Mie Doppler wind lidar for atmospheric measurements. I. Instrumental setup, validation, and first climatological results," Appl. Opt. **38**, 2410-2421 (1999).

14. C. Souprayen, A. Garnier, A. Hertzog, A. Hauchecorne, and J. Porteneuve, "Rayleigh-Mie Doppler wind lidar for atmospheric measurements. II. Mie scattering effect, theory, and calibration," Appl. Opt. **38**, 2422-2431 (1999).

15. C. Tepley, S. Sargoytchev, and C. Hines, "Initial Doppler Rayleigh lidar results from Arecibo," Geophys. Res. Lett. **18**, 167-170 (1991).

16. C. A. Tepley, S. I. Sargoytchev, and R. Rojas, "The Doppler Rayleigh lidar system at Arecibo," IEEE Trans. Geosci. Remote Sens. **31**, 36-47 (1993).

17. C. Tepley, "Neutral winds of the middle atmosphere observed at Arecibo using a Doppler Rayleigh lidar," J. Geophys. Res. **99**, 25781-25790 (1994).

18. B. M. Gentry, H. Chen, and S. X. Li, "Wind measurements with 355-nm molecular Doppler lidar," Opt. Lett. **25**, 1231-1233 (2000).

19. D. Rees, M. Vyssogorets, N. P. Meredith, E. Griffin, and Y. Chaxell, "The Doppler wind and temperature system of the ALOMAR lidar facility: overview and initial results," J. Atmos. Sol. Terr. Phys. **58**, 1827-1842 (1996).

20. U. von Zahn, G. von Cossart, J. Fiedler, K. H. Fricke, G. Nelke, G. Baumgarten, D. Rees, A. Hauchecorne, and K. Adolfsen, "The ALOMAR Rayleigh/Mie/Raman lidar: Objectives, configuration, and performance," Ann. Geophys. **18**, 815-833 (2000).

21. A. Stoffelen, J. Pailleux, E. Källén, J. M. Vaughan, L. Isaksen, P. Flamant, W. Wergen, E. Andersson, H. Schyberg, A. Culoma, R. Meynart, M. Endemann, and P. Ingmann, "The atmospheric dynamics mission for global wind field measurement," Bull. Am. Meteorol. Soc. **86**, 73-87 (2005).

22. O. Reitebuch, C. Lemmerz, E. Nagel, U. Paffrath, Y. Durand, M. Endemann, F. Fabre, and M. Chaloupy, "The airborne demonstrator for the direct-detection Doppler wind lidar ALADIN on ADM-Aeolus. Part I: Instrument design and comparison to satellite instrument," J. Atmos. Ocean. Technol. **26**, 2501-2515 (2009).

23. U. Paffrath, C. Lemmerz, O. Reitebuch, B. Witschas, I. Nikolaus, and V. Freudenthaler, "The airborne demonstrator for the direct-detection Doppler wind lidar ALADIN on ADM-Aeolus. Part II: Simulations and Rayleigh Receiver Radiometric performance," J. Atmos. Ocean. Technol. **26**, 2516-2530 (2009).

24. F. Shen, H. Cha, J. Dong, D. Kim, D. Sun, and S. O. Kwon, "Design and performance simulation of a molecular Doppler wind lidar," Chin. Opt. Lett. **7**, 593-597 (2009).

25. H. Xia, X. Dou, D. Sun, Z. Shu, X. Xue, Y. Han, D. Hu, Y. Han, and T. Cheng, "Mid-altitude wind measurements with mobile Rayleigh Doppler lidar incorporating system-level optical frequency control method," Opt. Express **20**, 15286-15300 (2012).

26. Y. Han, X. Dou, D. Sun, H. Xia, Z. Shu, "Analysis on wind retrieval methods for Rayleigh Doppler lidar," Opt. Eng. **53**, 061607 (2014).

27. X. Dou, Y. Han, D. Sun, H. Xia, Z. Shu, R. Zhao, M. Shangguan, and J. Guo, "Mobile Rayleigh Doppler lidar for wind and temperature measurements in the stratosphere and lower mesosphere," Opt. Express **22**, A1203-A1221 (2014).

28. R. Zhao, X. Dou, D. Sun, X. Xue, J. Zheng, Y. Han, T. Chen, G. Wang, and Y. Zhou, "Gravity waves observation of wind field in stratosphere based on a Rayleigh Doppler lidar," Opt. Express **24**, A581-A591 (2016).